Article

Dual PID Adaptive Variable Impedance Constant Force Control for Grinding Robot

Chong Wu, Kai Guo * and **Jie Sun**

Key Laboratory of High Efficiency and Clean Mechanical Manufacture of Ministry of Education, Department of Mechanical Engineering, Shandong University, Jinan 250061, China;
* Correspondence: kaiguo@sdu.edu.cn

Abstract: High-precision and low-overshoot force control are important to guarantee the material removal rate and surface quality of robot grinding. However, traditional force control methods are subjected to positional disturbance, stiffness disturbance, contact process nonlinearity, and force-position coupling, leading to difficulties in robot constant force control. Therefore, how to achieve smooth, stable, and high-precision constant force control is an urgent problem. To address this problem, a dual PID adaptive variable impedance control is established (DPAVIC). Firstly, PD control is used to compensate for the force error, and PID is used to update the damping parameters to compensate for the disturbance. Secondly, a nonlinear tracking differentiator is used to smooth the desired force and reduce the contact force overshoot. Then, the stability, convergence, and effectiveness of the force control algorithm are verified via theoretical analysis, simulations, and experiments. The force tracking error and overshoot of a conventional impedance controller (CIC), adaptive variable impedance control (AVIC), and DPAVIC are analyzed. Finally, the algorithm is used in grinding experiments on a thin-walled workpiece. The force tracking error is controlled within ± 0.2 N, and the surface roughness of the workpiece is improved to Ra 0.218 μm.

Keywords: robot grinding; constant force control; dual PID control; adaptive variable impedance

1. Introduction

In the manufacturing process of molds, aircraft panels, sculptures, etc., grinding and polishing are used to reduce the surface roughness and improve the machining accuracy [1,2]. However, most grinding and polishing operations are still performed manually, resulting in low manufacturing efficiency, poor workpiece surface quality, and worker health problems [3,4]. The automatic grinding and polishing processes represented by computer numerical control machine tools (CNCs) and industrial robots have become the main solutions [5,6]. CNCs not only have excellent stiffness and high precision positioning, but can also concurrently control trajectory, pose, and force [7]. However, the grinding space of CNCs is small, they have poor flexibility, and the machine tools need to be designed individually for large-scale special-shaped surfaces, which limit the application [8]. Robots have the advantages of a large working range, high flexibility, and have gradually become a research hot-spot in the field of grinding and polishing.

Robot grinding is a typical constrained operation. According to Preston's law, the amount of workpieces removed increases monotonically with the increase in grinding force, tool speed, and residence time, the most important of which is the control of the grinding force [9]. Therefore, controlling the robot end contact force is of great significance to improve the surface quality [10,11]. However, applying position-based industrial robots directly to grinding and polishing processes involving contact motion is not straightforward [2,12]. An accurate and smooth contact force control method is the key to realize high-quality automatic grinding and polishing of robots.

Robot end contact force control methods are mainly divided into passive force control [13,14] and active force control [15,16]. Passive force control is achieved through energy absorption or the storage of the auxiliary flexibility mechanism, and the robot is still in position control mode [17,18]. Typical force control devices mainly include voice coil motor actuators [19,20], parallel mechanism actuators [21,22], pneumatic actuators [23–25], mechanically flexible structures [26–29], force control joints [30], etc. Chen et al. [31] adopted a dual force sensor to decouple the dynamics between the macro robot, micro robot, and workpiece to achieve high-precision force control. However, passive force control requires the installation of an actuator at the robot end, which puts forward higher requirements for the design of the end actuator in the case of a limited end load of the robots. Therefore, active force control is more feasible.

Active force control is the use of designed control strategies to actively control force through the feedback of contact force information [32]. In the aspect of force control algorithms, the design of the force controller is the most important, and the common force control algorithms are impedance control [33,34] and hybrid position/force control [35,36]. For uncertain environments, that is, when the stiffness and position of the environment are unknown, it is difficult to obtain an accurate model, which makes it difficult to achieve high-precision force tracking. There are three main solutions: (1) Indirect adjustment of the reference trajectory: the basic method is to identify environmental information, including stiffness and position [37,38]. (2) Direct adjustment of the reference trajectory: the basic method is to update the reference trajectory with prior information [39,40]. However, this method ignores the dynamic physical characteristics of the robot and the environment and usually results in a large force tracking error. (3) Adaptive variable impedance control: this method adaptively adjusts the controller parameters according to force feedback information [41–43]. To improve the accuracy of force tracking, the researchers combined the adaptive algorithm with other force control methods to obtain better force control results [44]. Examples include fuzzy logic control [45], robust force control [46], optimal control [47], etc. Therefore, the key to establish a force tracking controller is to compensate for environmental disturbance, which is oriented to practical applications, and the control method should not be too complicated.

Force overshoot usually occurs when the robot end effector touches the workpiece. Although this problem only occurs in a short time, it will lead to poor system stability and low surface quality. Therefore, it is extremely important to ensure the stability of the system [15]. The nonlinear feedback control method is used to plan the trajectory and contact force simultaneously to reduce the force overshoot [48]. Roveda et al. [49] adopted an impedance shaping method to reduce the influence of force overshoot on system stability and achieve stable contact state transition. These methods usually require accurate estimates of the environmental position and stiffness, and this approach is difficult.

In this work, a dual PID adaptive impedance control method is proposed to achieve smooth, stable, and high-precision robot end contact force control. PD is used to compensate for the force error, and PID is used to update the damping parameters to compensate for the environmental uncertainty. A nonlinear tracking differentiator is used to reduce the impact of the transitional contact state. The interference term of the end 6-Dof force sensor is compensated using the least square method to ensure the accuracy of force control. The stability, convergence, and effectiveness of the force control algorithm are verified with theoretical analysis, simulations, and experiments. Furthermore, the thin-walled workpiece is used in a robot grinding experiment to verify the accuracy of force control.

The remainder of this paper is organized as follows: In Section 2, a nonlinear tracking differentiator is used to stabilize the contact transition state. In Section 3, a position-based dual PID adaptive impedance control method is established to compensate for the uncertainty of environment. In Section 4, the interference term of the 6-Dof force sensor is compensated for. The proposed method is verified in MATLAB/Simulink in Section 5. In Section 6, the effectiveness of the method is verified via force control and grinding experiments.

2. Modeling of Grinding System and Suppression of Contact Force Overshoot

A grinding robot system is established, as shown in Figure 1. A 7-Axis Franka Emika Panda robot is used; a Dynpick 6-Dof force sensor (Type: WEF-6A200-4-RC24, the force measurement range is ±200 N and the moment measurement range is ±4 Nm. Manufacturer: WACOH-TECH. City: Tokyo. Country: Japan.), an analog IO module (Type: NET6043-S, 8-Channel 0-10V analog input module with resolution of 16-Bit. Manufacturer: HKTECH. City: Zhengzhou. Country: China.) and a grinding tool are installed at the end of the robot.
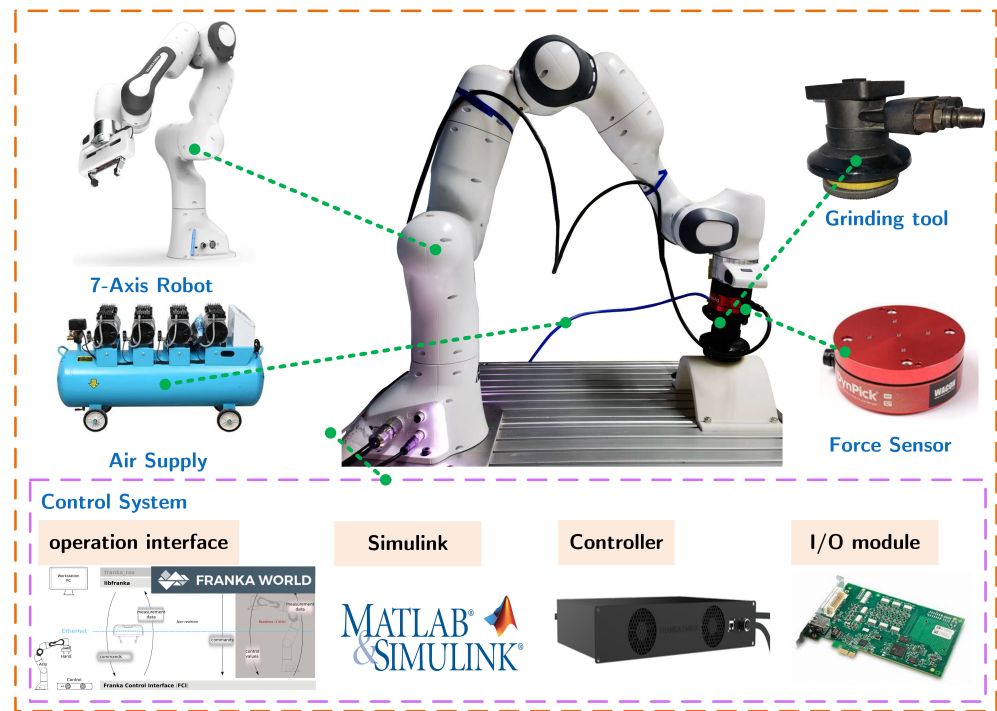

Figure 1. Robot grinding force control system.

As shown in Figure 2, with the robot and the workpiece set as a spring-damp-mass system, the contact process between the robot and the workpiece can be divided into three stages [50]. Figure 2a shows that the robot does not have contact with the workpiece, and Figure 2b shows the critical point of contact between the robot and the workpiece; the contact force is 0 N, and Figure 2c shows the full contact between the robot and the workpiece. In Figure 2d, From 0 to t_1 the contact force between the robot and the environment is 0. From t_1 to t_2, after a collision process, the contact force tends to be stable, but the collision process is short and nonlinear.
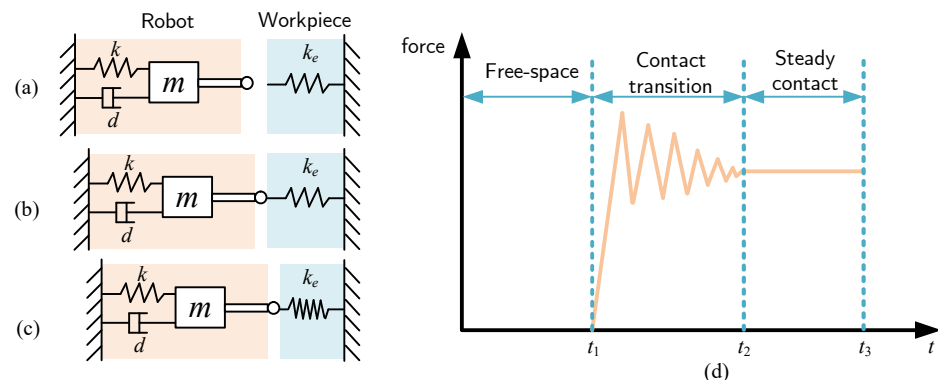

Figure 2. Contact behavior between robot and external environment. (**a**) No contact. (**b**) Critical point of contact. (**c**) The contact state. (**d**) The contact force during the contact process.

From Figure 2d, it can be found that the oscillation of the robot from the free state to the contact state is inevitable. Smooth adjustment of the robot grinding force will improve the stability and grinding quality. According to the design principle of ADRC, a nonlinear tracking differentiator (NTD) is used to smooth the step signal of the desired force signal in the transition stage. The control mode is shown in Figure 3.
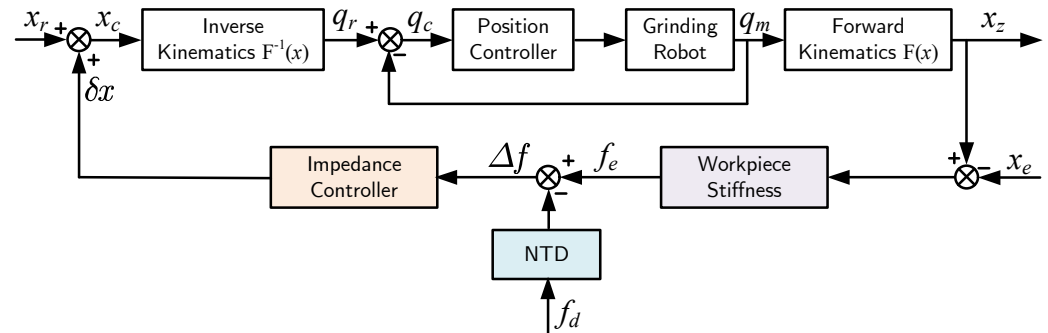

Figure 3. Robot end-contact-force transition state control.

Consider a two-order integrator series system:

$$\begin{cases} \dot{x}_1 = x_2 \\ \dot{x}_2 = u, |u| \leqslant r \end{cases} \tag{1}$$

where x_1 is the target transition signal, x_2 is the differential signal of the transition signal, r is the model parameter, and $r > 0$. If the control rate of the control parameter u is set as a nonlinear function, a nonlinear tracking differentiator can be obtained:

$$u(x_1, x_2) = -r \, \text{sign}\left(x_1 + \frac{x_2|x_2|}{2r}\right) \tag{2}$$

Considering that the control period of the grinding robot is 1 ms, NTD in discrete form is adopted:

$$\begin{cases} \text{fh} = \text{fhan}\,(x_1(k) - v_0(t), x_2(k), r, h) \\ x_1(k+1) = x_1(k) + t_s x_2(k) \\ x_2(k+1) = x_2(k) + t_s \text{fh} \end{cases} \tag{3}$$

where t_s is sampling time. The fhan function is as follows:

$$\begin{cases} d = rh^2 \\ a_0 = hx_2 \\ y = x_1 + a_0 \\ a_1 = \sqrt{d(d + 8|y|)} \\ a_2 = a_0 + \text{sign}(y)(a_1 - d)/2 \\ a = (a_0 + y)\,\text{fsg}(y, d) + a_2(1 - \text{fsg}(y, d)) \\ \text{fhan} = -r\left(\frac{a}{d}\right)\text{fsg}(a, d) - r\,\text{sign}(a)(1 - \text{fsg}(a, d)) \end{cases} \tag{4}$$

where $\text{fsg}(x, d) = (\text{sign}(x + d) - \text{sign}(x - d))/2$, h is the filter factor, and h is slightly larger than the sampling time t_s.

To verify the NTD smoothing effect, we set the parameters of the impedance controller to $m = 1$ kg, $b = 50$ N/(m/s), and $k = 50$ N/m. The external environment stiffness was set to 2000 N/m. In NTD, $r = 500$, $h = 0.01$, and the simulation time was 4 s. In Figure 4a , the 0–2 s desired force is -3 N, and the 2–4 s desired force is -5 N. In Figure 4b, after NTD smoothing, the overshoot of the force is significantly reduced. The overshoot is reduced from 18.57% to 0.25% in 0–2 s. The overshoot is reduced from 5% to 0.2% in 2–4 s. It is found that the response time is slightly increased, but the system stability is enhanced, which is of great significance for the improvement of workpiece processing quality and system

stability. It is verified in the force control system shown in Figure 1; the experimental results are basically consistent with the simulation results, as shown in Figure 4c.
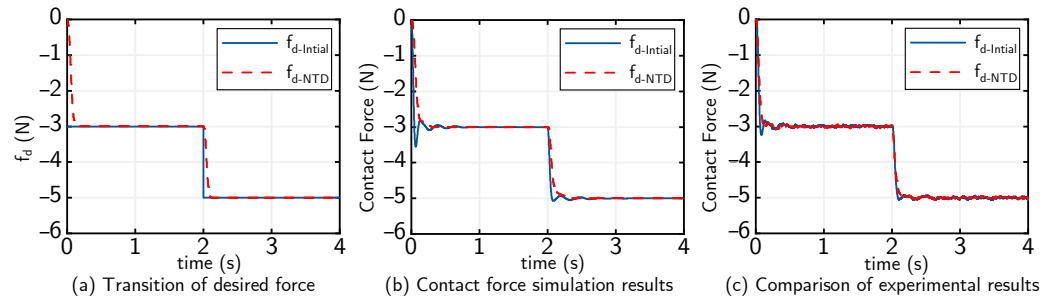

Figure 4. Simulation and experimental results of robot end contact state transition.

3. Position-Based Adaptive Impedance Control

3.1. Dual PID Adaptive Variable Impedance Control

Since industrial robots generally only open a position loop, it is difficult to obtain accurate values of workpiece stiffness and position. Therefore, position-based impedance control avoids the consideration of dynamics. According to the target impedance to calculate the position deviation, compensating for the reference position achieves accurate force control. The contact state of the robot is shown in Figure 5.
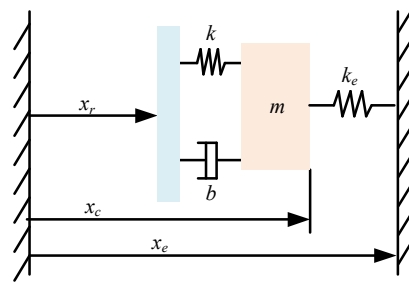

Figure 5. The state of contact between the workpiece and the end effector.

The position-based impedance control strategy is shown in Figure 3, where X_r, X_c, and X_z are represented as reference trajectory, command trajectory, and robot end output trajectory, respectively. Assume that the robot's controller performs well, namely, $X_c = X_z$. The contact position between the end and the environment is $E = X_z - X_r = X_c - X_r$. The contact environment stiffness is K_e; the desired contact force is F_d. The contact force between the end of the robot and the environment can be simplified as $F_e = K_e(X_e - X_z) = K_e(X_e - X_c)$. Then, the end contact force error is:

$$\Delta F = F_e - F_d \tag{5}$$

In general, the impedance model is represented by a second-order transfer function $K(s)$, $K(s) = \frac{1}{Ms^2 + Bs + K}$. The dynamic relationship between force error ΔF and position disturbance E is as follows:

$$M\frac{d^2E(t)}{dt^2} + B\frac{dE(t)}{dt} + KE(t) = \Delta F(t) \tag{6}$$

where M is the mass of the target impedance, B is the damping of the target impedance, and K is the stiffness of the target impedance. Thus, the reference position can be modified by position perturbation E:

$$X_c = X_r + E = X_r + \Delta F \cdot K(s) \tag{7}$$

In the robot grinding process, only one dimension of the end is considered. Therefore, we rewrite Equation (6) as:

$$\Delta f = f_e - f_d = k_e(x_e - x_z) - f_d = k_e x_e - k_e(x_r + k(s)\Delta f) - f_d \tag{8}$$

where Δf is the force error of one dimension. f_e is the contact force of one dimension. f_d is the desired force of one dimension. k_e is the environmental stiffness of one dimension. x_e is the environmental position of one dimension. x_z is the output position of the robot end in the force control direction. x_r is the reference position of one dimension. $k(s)$ is a second-order transfer function in one dimensional direction.

Then, Equation (8) can be rewritten as:

$$\Delta f = \frac{ms^2 + bs + k}{ms^2 + bs + k + k_e}[k_e(x_e - x_r) - f_d] \tag{9}$$

The steady-state force tracking error Δf_{ss} is obtained as follows:

$$\Delta f_{ss} = \Delta f_{s \to 0} = \frac{k}{k + k_e}[k_e(x_e - x_r) - f_d] \tag{10}$$

If the force tracking error converges to 0 under steady-state conditions, the following conditions need to be met:

$$k = 0, \text{ or } , x_r = x_e - \frac{f_d}{k_e} \tag{11}$$

According to Equation (11), the steady-state error of 0 can be satisfied under the condition that the environmental position x_e and the contact stiffness k_e are known. However, in the robot grinding process, accurate x_e and k_e values are not easy to obtain. Therefore, setting the stiffness term of the impedance controller to 0 can compensate for the environmental uncertainty. Since the position of the environment is replaced by the initial environmental position x_e instead of the reference position x_r, the position disturbance is $e = x_z - x_e$:

Equation (8) can be expressed as:

$$\Delta f = f_e - f_d = m\ddot{e} + b\dot{e} \tag{12}$$

where $\ddot{e} = \ddot{x}_z - \ddot{x}_e$ and $\dot{e} = \dot{x}_z - \dot{x}_e$

Through the above analysis, if it is flat grinding, namely, $\ddot{x}_e = \dot{x}_e = 0$, then $\Delta f_{ss} = 0$. However, when grinding a non-flat surface, namely, $\dot{x}_e \neq 0$ or $\ddot{x}_e \neq 0, \dot{x}_e \neq 0$, which needs to estimate the environmental position $\hat{x}_e$. The relationship between the estimated environmental position $\hat{x}_e$ as the reference position x_e and the estimated deviation $\delta\hat{x}_e$ can be expressed as:

$$\hat{x}_e = x_e - \delta\hat{x}_e \tag{13}$$

Thus, the estimated position disturbance $\hat{e}$ is:

$$\hat{e} = e + \delta\hat{x}_e \tag{14}$$

Substituting Equation (14) into Equation (12):

$$\Delta f = m\ddot{\hat{e}} + b\dot{\hat{e}} = m(\ddot{e} + \delta\ddot{x}_e) + b(\dot{e} + \delta\dot{x}_e) \tag{15}$$

In Equation (15), $\dot{\hat{e}}$ and $\ddot{\hat{e}}$ are time-varying parameters, first-order and second-order differentiation for the estimated position disturbance, respectively. To achieve a steady state quickly and a simple control strategy, adaptive impedance control can eliminate steady-state errors. However, if modifying the mass parameter, the system may oscillate, so the damping parameter can be adjusted according to the force tracking error.

Adaptive impedance controller control law is:

$$\Delta f = m\ddot{\hat{e}}(t) + (b + \Delta b(t))\dot{\hat{e}}(t) \tag{16}$$

$\Delta b(t)$ can be expressed as:

$$\begin{cases} \Delta b(t) = \frac{b}{\hat{\dot{e}}(t)+\lambda}\Gamma(t) \\ \Gamma(t) = \Gamma(t-t_s) + \sigma\frac{f_e(t-t_s)-f_r(t-t_s)}{b} \end{cases} \tag{17}$$

where t_s is the sampling time, σ is the parameter update rate, and $0 < \sigma < 1$, which plays a decisive role in the stability and force tracking effect of the adaptive impedance controller. When σ is too large, the system will overshoot or oscillate, and σ is too small to track environmental disturbances and cannot achieve the desired force tracking. $\lambda = 0.1$ is the adjustment factor, which ensures that $\Delta b(t)$ does not oscillate or tend to infinity because the denominator is too small.

Although NTD is used to mitigate the end overshoot of the robot, it can be found from Figure 4 that there is still overshoot, and improper parameter selection of the adaptive impedance controller will also affect the stability and tracking effect of the system. When the selected mass parameter and stiffness parameter are too large, it will lead to system oscillation, which seriously impede the stability of this system. Moreover, when the stiffness parameter is selected, it will lead to a lower accuracy of the system force control, and it is difficult to ensure that the system's steady-state error converges to 0. Therefore, PD is used to reduce force tracking, and PID is used to adjust the adaptive update rate. They are real-time synchronous control. The control strategy is shown in Figure 6, and Equation (16) is rewritten as:

$$m\ddot{\hat{e}}(t) + (b + \Delta b(t))\dot{\hat{e}}(t) = k_p\Delta f(t) + k_d\Delta\dot{f}(t) = \Delta f_{PD}(t) \tag{18}$$

where k_p and k_d are the coefficients of the PD controller, respectively.

Equation (17) is rewritten as:

$$\begin{cases} \Delta b(t) = \frac{b}{\hat{\dot{e}}(t)+\lambda}\Gamma(t) \\ \Gamma(t) = \Gamma(t-t_s) - \sigma\frac{k_p\Delta f(t-t_s)+k_d\Delta\dot{f}(t-t_s)+k_i\int_0^{t-t_s}\Delta f(\tau)d\tau}{b} \end{cases} \tag{19}$$

Figure 6. Dual PID adaptive variable impedance control.

To facilitate the control of robots, Equation (18) can be converted into a discrete format:

$$\begin{cases} \delta\ddot{x}(t) = m^{-1}[\Delta f_{PD}(t) - (b + \Delta b(t))\delta\dot{x}(t-1)] \\ \delta\dot{x}(t) = \delta\dot{x}(t-1) + \delta\ddot{x}(t) \cdot t_s \\ \delta x(t) = \delta x(t-1) + \delta\dot{x}(t) \cdot t_s \\ x_c(t) = x_r(t) + \delta x(t) \end{cases} \tag{20}$$

3.2. Stability and Convergence Analysis

To ensure the stability of the controller, the steady-state error of the force tracking converges to zero. Here is the proof.

Substituting Equation (19) into Equation (18):

$$k_p\Delta f(t) + k_d\Delta\dot{f}(t) = m\ddot{\hat{e}}(t) + b\dot{\hat{e}}(t) + b\Gamma(t - t_s) - \sigma\left(\Delta f(t - t_s) + \Delta\dot{f}(t - t_s) + k_i\int_0^{t-t_s}\Delta f(\tau)d\tau\right) \tag{21}$$

Let $\hat{e} = e + \delta\hat{x}_e, \Delta f(t) = f_e(t) - f_d(t)$,

$$k_p(f_e(t) - f_d(t)) + k_d(\dot{f}_e(t) - \dot{f}_d(t)) = m(\ddot{e}(t) + \delta\ddot{\hat{x}}_e(t)) + b(\dot{e}(t) + \delta\dot{\hat{x}}_e(t)) + b\Gamma(t - t_s) - \\ \sigma\left(\Delta f(t - t_s) + \Delta\dot{f}(t - t_s) + k_i\int_0^{t-t_s}\Delta f(\tau)d\tau\right) \tag{22}$$

where $e = x_z - x_e, f_e = k_e(x_e - x_z) = -k_e e, \dot{e} = -\frac{\dot{f}_e}{k_e}, \ddot{e} = -\frac{\ddot{f}_e}{k_e}$.

$$-m\frac{\ddot{f}_e(t)}{k_e} - b\frac{\dot{f}_e(t)}{k_e} + b\Gamma(t - t_s) - \sigma\left(\Delta f(t - t_s) + \Delta\dot{f}(t - t_s) + k_i\int_0^{t-t_s}\Delta f(\tau)d\tau\right) - k_p(f_e(t) - f_d(t)) - \\ k_d(\dot{f}_e(t) - \dot{f}_d(t)) = -m\delta\ddot{\hat{x}}_e(t) - b\delta\dot{\hat{x}}_e(t) \tag{23}$$

Let $\hat{f}_e(t) = k_e\delta x_e(t), \delta x_e(t) = \frac{\hat{f}_e(t)}{k_e}, \delta\dot{x}_e(t) = \frac{\dot{\hat{f}}_e(t)}{k_e}, \delta\ddot{x}_e(t) = \frac{\ddot{\hat{f}}_e(t)}{k_e}$,

$$m(\ddot{f}_d(t) - \ddot{f}_e(t)) + b(\dot{f}_d(t) - \dot{f}_e(t)) + k_e b\Gamma(t - t_s) - \sigma k_e\left(\Delta f(t - t_s) + \Delta\dot{f}(t - t_s) + k_i\int_0^{t-t_s}\Delta f(\tau)d\tau\right) - \\ k_p k_e(f_e(t) - f_d(t)) - k_d k_e(\dot{f}_e(t) - \dot{f}_d(t)) = m(\ddot{f}_d(t) - \ddot{\hat{f}}_e(t)) + b(\dot{f}_d(t) - \dot{\hat{f}}_e(t)) \tag{24}$$

Let $\psi(t) = f_d(t) - f_e(t), \Phi(t) = f_d(t) - \hat{f}_e(t)$:

$$m\ddot{\psi}(t) + b\dot{\psi}(t) + k_e b\Gamma(t - t_s) - \sigma k_e\left(\Delta f(t - t_s) + \Delta\dot{f}(t - t_s) + k_i\int_0^{t-t_s}\Delta f(\tau)d\tau\right) + k_p k_e\psi(t) + k_d k_e\dot{\psi}(t) \\ = m\ddot{\Phi}(t) + b\dot{\Phi}(t) \tag{25}$$

According to the dispersion principle, the *n*-th element in Γ can be expressed as:

$$b\Gamma(t - t_s) = b\Gamma(t - (n+1)t_s) + \sigma\psi(t - (n+1)t_s) + \cdots + \sigma\psi(t - 2t_s) \tag{26}$$

Supposing the initial value Γ is 0, namely, $\Gamma(t - (n+1)t_s)$, substituting Equation (26) into Equation (25):

$$\frac{\psi(s)}{\Phi(s)} = \frac{ms^2 + bs}{ms^2 + bs + k_p k_e + k_d k_e s + \sigma k_e\left(e^{-(n+1)t_s s} + \cdots + e^{-t_s s} + e^{-t_s s}s + \frac{1}{s}k_i\right)} \tag{27}$$

The characteristic equation in Equation (27) is:

$$ms^2 + bs + k_p k_e + k_d k_e s + \sigma k_e\left(e^{-(n+1)t_s s} + \cdots + e^{-t_s s} + e^{-t_s s}s + \frac{1}{s}k_i\right) = 0 \tag{28}$$

Supposing n is large enough, it can be represented as $\sum\limits_{n=1}^{\infty} e^{-nt_s s} = \frac{e^{-t_s s}}{1-e^{-t_s s}}$. Furthermore, when the sampling time t_s is small enough, Taylor expansion is used so that $e^{-t_s s} \approx 1 - t_s s$. The system characteristic Equation (28) is simplified as:

$$t_s(m - \sigma k_e t_s)s^3 + t_s(b + k_d k_e + \sigma k_e)s^2 + t_s(k_p k_e - \sigma k_e)s + \sigma k_e + \sigma k_e t_s k_i = 0 \qquad (29)$$

The Routh table is obtained according to Routh criterion:

$$
\begin{array}{lll}
s^3 & t_s(m - \sigma k_e t_s) & t_s(k_p k_e - \sigma k_e) \\
s^2 & t_s(b + k_d k_e + \sigma k_e) & \sigma k_e + \sigma k_e t_s k_i \\
s^1 & \frac{k_e t_s(k_p - \sigma)(b + k_d k_e + \sigma k_e) - \sigma k_e(m - \sigma k_e t_s)(1 + t_s k_i)}{(b + k_d k_e + \sigma k_e)} & 0 \\
s^0 & \sigma k_e + \sigma k_e t_s k_i & 0
\end{array}
\qquad (30)
$$

Then, the sufficient and necessary condition for the stability of the system is that all coefficients of the characteristic equation are positive and the first column of the Routh table is positive, so:

$$
\begin{cases}
t_s(m - \sigma k_e t_s) > 0 \\
\frac{k_e t_s(k_p - \sigma)(b + k_d k_e + \sigma k_e) - \sigma k_e(m - \sigma k_e t_s)(1 + t_s k_i)}{(b + k_d k_e + \sigma k_e)} > 0 \\
t_s(k_p k_e - \sigma k_e) > 0 \\
\sigma k_e + \sigma k_e t_s k_i > 0
\end{cases}
\qquad (31)
$$

If the controller parameters are within the range given by Equation (31), the system is stable, and for stable systems, the steady-state error e_{ss} can be obtained.

$$e_{ss} = \lim_{t \to \infty} e(t) = \lim_{s \to 0} sE(t) = \lim_{s \to 0} s(\psi(s) - \Phi(s)) \qquad (32)$$

To verify the stability of the system, the input signal is a step signal, namely, $\Phi(s) = \frac{1}{s}$.

$$\lim_{s \to 0} s(\psi(s) - \Phi(s)) = -1 \qquad (33)$$

Then,

$$\lim_{s \to 0} s(\psi(s)) = 0, \lim_{t \to 0}(\psi(t)) = 0 \qquad (34)$$

Therefore, under the influence of external interference, the force tracking error converges to zero.

4. 6-Dof Force Sensor Gravity Compensation Strategy

The gravity of the grinding tool generates components of force and moment in the sensor coordinate system. The force and moment F_m measured with the 6-Dof force sensor include: The grinding force F_e between the grinding tool and the workpiece, the gravity of the grinding tool F_G, the inertial force F_i generated by the grinding tool because of the movement (since the feed speed of the grinding tool changes very little, so that $F_i = 0$), and the sensor zero drift F_0:

$$^S F_m = {}^S F_e + {}^S F_G + {}^S F_i + {}^S F_0 \qquad (35)$$

where the superscript $^S \bullet$ indicates that the reference coordinate system of the force is in the sensor coordinate system {S}.

Figure 7 shows the relationship between the world coordinate system {D}, the robot base coordinate system {B}, the end flange coordinate system {E}, the force sensor coordinate system {S}, and the grinding tool coordinate system {T}. The barycenter of the grinding tool is represented as $^S o(x, y, z)$ in the {S} system. Using pins to maintain

the parallel relationship between the axes of the {S} and {E} system, the homogeneous transformation matrix $^{B}_{S}T$ from {S} to {B} is:

$$^{B}_{S}T = \begin{bmatrix} ^{B}_{S}R & ^{B}_{S}P \\ 0 & 1 \end{bmatrix} \tag{36}$$

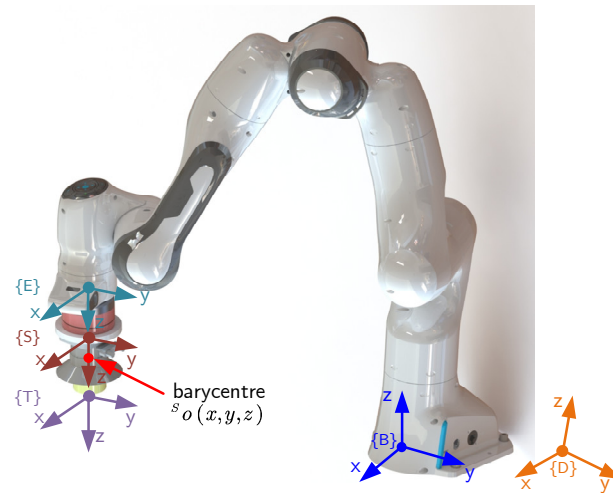where $^{B}_{S}R$ is the rotation matrix and $^{B}_{S}P$ is the vector of the sensor origin in the {S} system.

Figure 7. Gravity compensation modeling.

When there is no contact between the grinding tool and the workpiece, the sensor output signal is composed of the tool gravity and the sensor zero drift:

$$\begin{cases} ^{S}F_{mx} = ^{S}F_{Gx} + F_{x0} \\ ^{S}F_{my} = ^{S}F_{Gy} + F_{y0} \\ ^{S}F_{mz} = ^{S}F_{Gz} + F_{z0} \\ ^{S}M_{mx} = ^{S}M_{Gx} + M_{x0} \\ ^{S}M_{my} = ^{S}M_{Gy} + M_{y0} \\ ^{S}M_{mz} = ^{S}M_{Gz} + M_{z0} \end{cases} \tag{37}$$

where $^{S}F_{mx}, ^{S}F_{my}, ^{S}F_{mz}, ^{S}M_{mx}, ^{S}M_{my}$ and $^{S}M_{mz}$ are the force and moment signals of the 6-Dof force sensor, respectively.

Using the tool gravity and barycenter to obtain the torque that acts on the {S} system of the force sensor:

$$\begin{cases} ^{S}M_{mx} = ^{S}F_{mz}y - ^{S}F_{my}z + M_{x0} + F_{y0}z - F_{z0}y \\ ^{S}M_{my} = ^{S}F_{mx}z - ^{S}F_{mz}x + M_{y0} + F_{z0}x - F_{x0}z \\ ^{S}M_{mz} = ^{S}F_{my}x - ^{S}F_{mx}y + M_{z0} + F_{x0}y - F_{y0}x \end{cases} \tag{38}$$

Rewriting Equation (38) in matrix form:

$$^{S}M_m = ^{S}F_m \cdot A \tag{39}$$

where $A = [x, y, z, a_1, a_2, a_3]^T,$ $\begin{cases} a_1 = M_{x0} + F_{y0}z - F_{z0}y \\ a_2 = M_{y0} + F_{z0}x - F_{x0}z \\ a_3 = M_{z0} + F_{x0}y - F_{y0}x \end{cases},$

$$^{S}F_m = \begin{bmatrix} 0 & ^{S}F_{mz} & -^{S}F_{my} & 1 & 0 & 0 \\ -^{S}F_{mz} & 0 & ^{S}F_{mx} & 0 & 1 & 0 \\ ^{S}F_{my} & -^{S}F_{mx} & 0 & 0 & 0 & 1 \end{bmatrix}$$

Selecting N different poses of the robot and using the least squares solution:

$$A = \left({}^{S}F_{m}^{\mathrm{T}} \cdot {}^{S}F_{m}\right)^{-1} \cdot {}^{S}F_{m}^{\mathrm{T}} \cdot {}^{S}M_{m} \tag{40}$$

The coordinate value x, y, z of tool barycenter and constant a_1, a_2, a_3 in {S} system is obtained.

To obtain the component of the grinding tool in the {B} system, it is necessary to consider the relationship between the {B} system and the {D} system. When the {B} system rotates around the z axis of the {D} system, there is no effect on the force sensor output. Consider that the {B} system rotates around the x-axis and the y-axis of the {D} system. Then, the rotation matrix ${}^{D}_{B}R$ between the {B} system and the {D} system is:

$$
{}^{D}_{B}R =
\begin{bmatrix}
1 & 0 & 0 \\
0 & \cos\theta_1 & -\sin\theta_1 \\
0 & \sin\theta_1 & \cos\theta_1
\end{bmatrix}
\cdot
\begin{bmatrix}
\cos\theta_2 & 0 & \sin\theta_2 \\
0 & 1 & 0 \\
-\sin\theta_2 & 0 & \cos\theta_2
\end{bmatrix}
\tag{41}
$$

where θ_1 and θ_2 are the angle around the x-axis and y-axis of the {D} system, respectively.

The component force of the grinding tool gravity G in the {S} system can be represented by the robot homogeneous transformation matrix:

$$
{}^{S}G =
\begin{bmatrix}
{}^{S}F_{Gx} \\
{}^{S}F_{Gy} \\
{}^{S}F_{Gz}
\end{bmatrix}
= {}^{S}_{B}R\,{}^{B}_{D}R\,{}^{D}G = {}^{S}_{B}R
\begin{bmatrix}
G\cos\theta_1 \sin\theta_2 \\
-G\sin\theta_1 \\
-G\cos\theta_1 \cos\theta_2
\end{bmatrix}
\tag{42}
$$

Let $\begin{cases} b_x = G\cos\theta_1 \sin\theta_2 \\ b_y = -G\sin\theta_1 \\ b_z = -G\cos\theta_1 \cos\theta_2 \end{cases}$.

According to Equation (37) and Equation (42):

$$
\begin{bmatrix}
{}^{S}F_{mx} \\
{}^{S}F_{my} \\
{}^{S}F_{mz}
\end{bmatrix}
=
\begin{bmatrix}
{}^{S}F_{Gx} \\
{}^{S}F_{Gy} \\
{}^{S}F_{Gz}
\end{bmatrix}
+
\begin{bmatrix}
F_{x0} \\
F_{y0} \\
F_{z0}
\end{bmatrix}
= {}^{B}_{S}R^{T}
\begin{bmatrix}
b_x \\
b_y \\
b_z
\end{bmatrix}
+
\begin{bmatrix}
F_{x0} \\
F_{y0} \\
F_{z0}
\end{bmatrix}
\tag{43}
$$

Rewriting Equation (43) in matrix form:

$$
\begin{bmatrix}
{}^{S}F_{mx} \\
{}^{S}F_{my} \\
{}^{S}F_{mz}
\end{bmatrix}
=
\begin{bmatrix}
{}^{B}_{S}R^{T} & | & I
\end{bmatrix}
\begin{bmatrix}
b_x \\
b_y \\
b_z \\
F_{x0} \\
F_{y0} \\
F_{z0}
\end{bmatrix}
\tag{44}
$$

Taking N different poses, we use Equation (44) to construct the equations and rewrite them as:

$$
{}^{S}F_{m} = {}^{B}_{S}R_{I} \cdot B
\tag{45}
$$

The least square solution of Equation (45) can be obtained as:

$$
B = \left({}^{B}_{S}R_{I}^{T}\,{}^{B}_{S}R_{I}\right)^{-1} \cdot {}^{B}_{S}R_{I}^{T} \cdot {}^{S}F_{m}
\tag{46}
$$

Then, the constant value of $b_x, b_y, b_z, F_{x0}, F_{y0}$ and F_{z0} is solved and, combined with Equation (39), the torque zero drift values ${}^{S}M_{mx0}, {}^{S}M_{my0}$ and ${}^{S}M_{mz0}$ of the 6-Dof force sensor can be obtained.

The gravity of the grinding tool is as follows: $G = \sqrt{b_x^2 + b_y^2 + b_z^2}$.

The angle value between the {B} system and the {D} system is as follows: $\theta_1 = \arcsin\left(-\frac{b_y}{g}\right), \theta_2 = \arcsin\left(-\frac{b_x}{b_z}\right)$.

The identification results in Tables 1 and 2 were obtained by selecting 10 groups of poses. The true gravity of the grinding tool is 8.542 N, which is only 0.414 N different from the identification result. We selected a trajectory and performed real-time gravity compensation. Figure 8 shows the compensation results; the maximum disturbance after compensation is less than 0.1 N and 0.03 N·m, which verifies the accuracy and effect of gravity compensation.

Table 1. The result of end effector gravity identification.

Gravity (N)	x (m)	y (m)	z (m)	θ_1 (°)	θ_2 (°)
8.956	−0.0020	−0.0053	0.0455	0.8052	1.8096

Table 2. The result of sensor zero drift identification.

Zero Drift	F_{x0} (N)	F_{y0} (N)	F_{z0} (N)	M_{x0} (Nm)	M_{y0} (Nm)	M_{z0} (Nm)
Value	0.6382	−0. 4779	0.5209	0.0295	0.0134	−0.0379
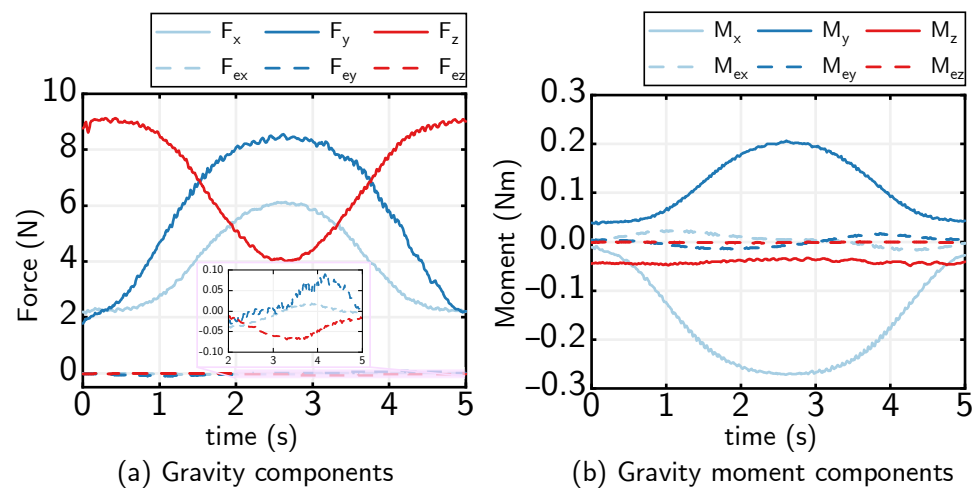
Figure 8. Comparison of sensor signals before ($F_\bullet$, $M_\bullet$) and after ($F_{e\bullet}$, $M_{e\bullet}$) compensation.

5. Controller Simulation Verification

Constant impedance control (CIC), adaptive variable impedance control (AVIC), and DPAVIC algorithms were used to verify the superiority and feasibility of the methods. The simulation system was established in MATLAB R2022b/Simulink, and the robot toolbox was used to establish the dynamics model of Franka Emika Panda. Table 3 shows the simulation parameters.

Table 3. Simulation parameters.

Parameters	Value
m(kg)	1.0
b(N/(m/s))	50
k(N/m)	0
k_e(N/m)	2000
t_s(ms)	1

The force control simulation was performed on the curved surface shown in Figure 9a. In the force controller, $k_p = 0.6, k_d = 0.4, k_i = 0.01, \sigma = 0.01, r = 500, h = 0.01$, and the desired force is $f_d = -5$N. As can be seen in Figure 9b, the force tracking errors of CIC

and AVIC both exceed the range of ±0.2 N. DPAVIC shows superior performance in the force tracking effect, and the force tracking error is within the range of ±0.2 N. Because the force overshoot is suppressed by NTD and PD in force tracking controllers, the overshoot of force is reduced from 52.34% to 8.3% compared with that in CIC. The force control effect is also simulated when the workpiece stiffness due to disturbance, as shown in Figure 10a, and it can be found from Figure 10b that both CIC and AVIC have large force fluctuations, while the force error of the method proposed in this paper is stable within the range of ±0.2 N. Therefore, the DPAVIC method can effectively compensate for the force tracking errors caused by position and stiffness disturbance.

(a) Contact Position

(b) Contact force response
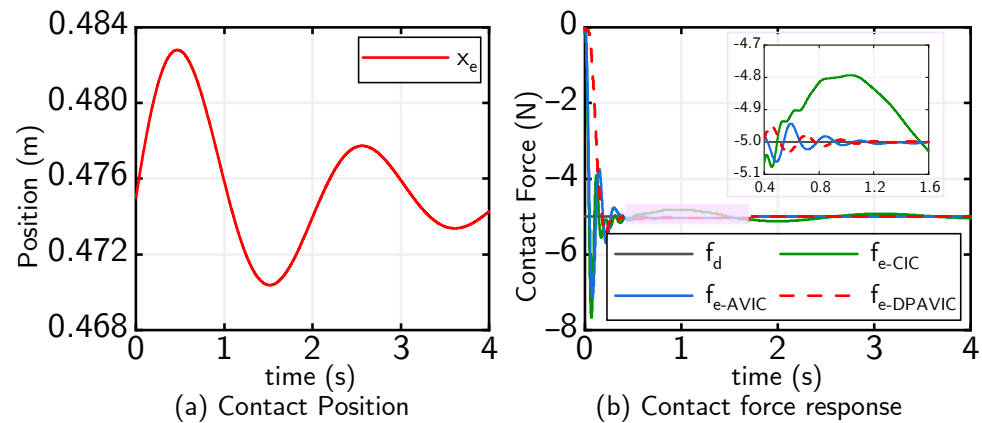
Figure 9. Force tracking results of curved surface.

(a) Contact Stiffness

(b) Contact force response
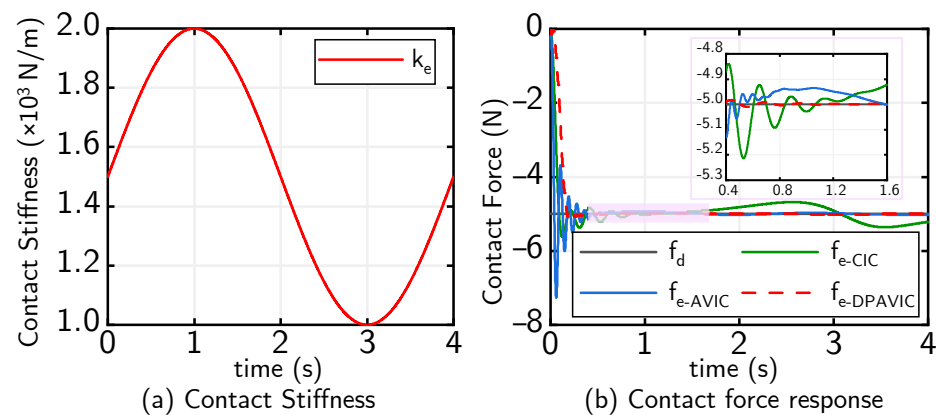
Figure 10. Force tracking results with the stiffness disturbance.

6. Experimental Study

To verify the performance of the proposed control strategy, a robot force control platform is established, as shown in Figure 11. Programming is performed in a MATLAB/Simulink environment using Simulink S-function block. The robot control frequency is 1KHz. The HKTECH NET6043-S analog IO module is connected to the robot controller through cables, the grinding force is read through the Simulink UDP module of the Industrial Personal Computer, and the grinding force signal is fed back to the robot control algorithm. Multiple groups of force control experiments are carried out on a flat surface, slope surface, and large curvature surface, respectively, as shown in Figure 12. Finally, the grinding experiment is carried out on a thin-wall aluminum alloy 7050-T6 workpiece. The results of CIC, AVIC, and DPAVIC on the end force tracking are discussed.
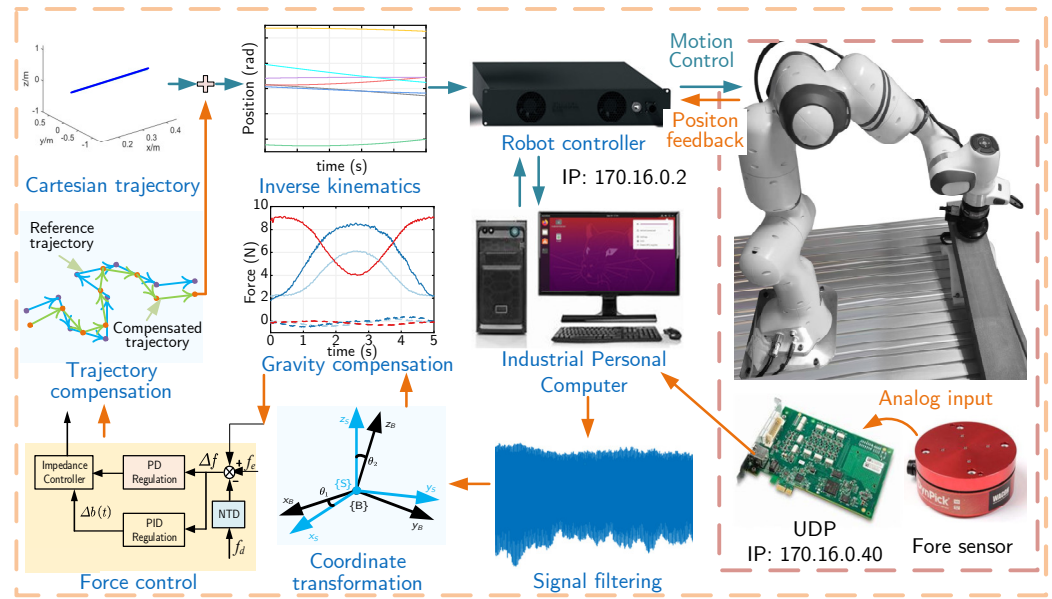
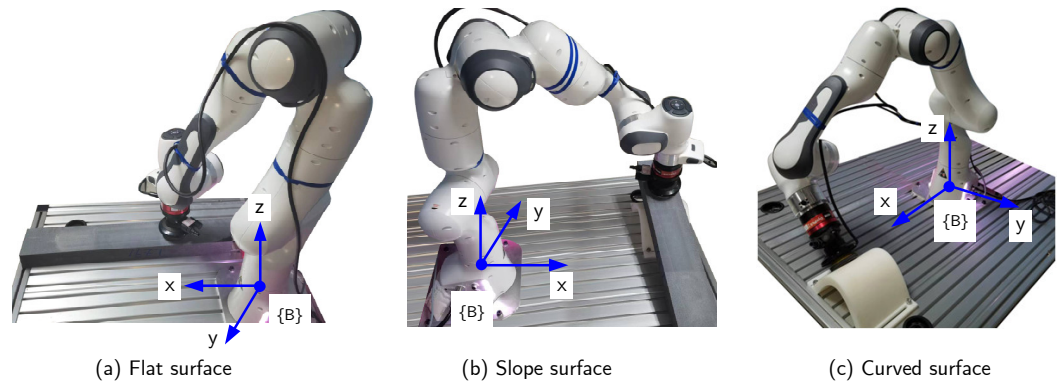**Figure 11.** Experimental setup for robot grinding force control.

(a) Flat surface

(b) Slope surface

(c) Curved surface

Figure 12. Force control platform.

6.1. Flat Surface Constant Force Control

The force control experiment was carried out on a flat surface, as shown in Figure 12a. The end of the robot moved 0.3 m in the x direction, and the force control direction was in the z direction of the end effector. The desired force was set as $f_d = -5$ N, and the running time was 10 s. The control parameters of CIC, AVIC, and DPAVIC were set as follows:

CIC: $m = 1, b = 10, k = 0$.

AVIC: $m = 1, b = 8, k = 0, \sigma = 0.003$.

DPAVIC: $m = 1, b = 5, k = 0, \sigma = 0.003, k_p = 0.4, k_d = 0.1, k_i = 0.001, r = 100, h = 0.01$.

Figure 13 shows the robot end contact force control and end compensation displacement. It can be found that when CIC and AVIC are adopted, the overshoot of the system is large, 34.31% and 13.54% respectively, the force control error is 0.409 N and 0.25 N, and the adjustment time is long. When the DPAVIC force control strategy is adopted, the overshoot is 1.35% and the force control error is within ± 0.2 N.
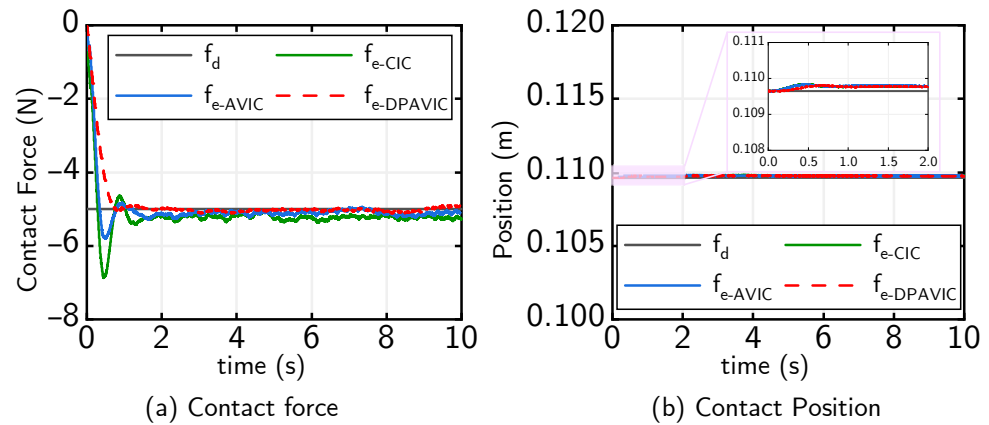
Figure 13. Force control results of flat surface.

6.2. Slope Surface Constant Force Control

The end contact force was controlled on the slope surface shown in Figure 12b. The desired force was set as $f_d = -5$ N and the running time was 10 s. The control parameters of the CIC, AVIC, and DPAVIC methods were set as follows:

CIC: $m = 1, b = 8, k = 0$.

AVIC: $m = 1, b = 5, k = 0, \sigma = 0.003$.

DPAVIC: $m = 1, b = 5, k = 0, \sigma = 0.005, k_p = 0.4, k_d = 0.05, k_i = 0.001, r = 100, h = 0.01$.

Figure 14 shows the control response curves of the end compensation displacement and the end contact force. It can be found that when CIC and AVIC are used, the overshoot of the system is 29.46% and 12.45%, respectively, and the force control error is 0.331 N and 0.247 N. When the DPAVIC force control strategy is adopted, the overshoot is less than 1.02%, and the error is within ± 0.2 N.
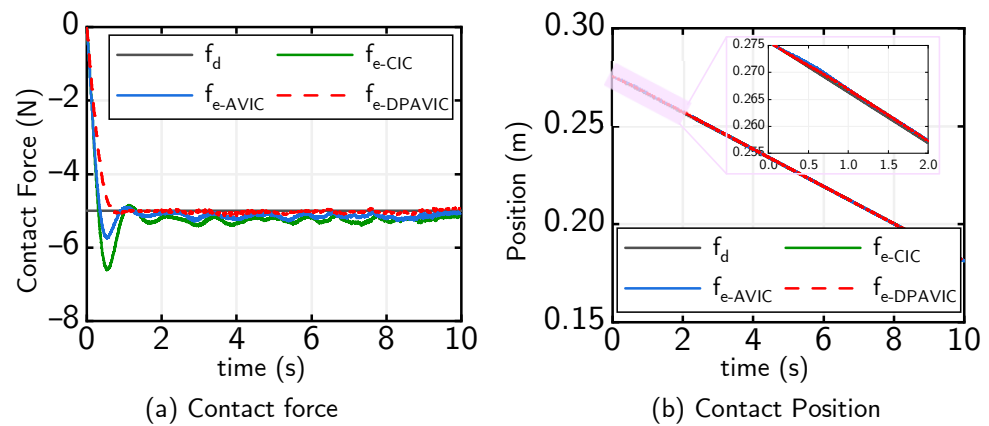

Figure 14. Force control results of slope surface.

6.3. Large Curvature Surface Constant Force Control

To ensure the force control effectiveness of the force control algorithm for curved surface parts, the force control platform shown in Figure 12c was adopted. The desired contact force was set as $f_d = -5$ N and the running time was 10 s. The control parameters of the CIC, AVIC, and DPAVIC methods were set as:

CIC: $m = 1, b = 8, k = 0$.

AVIC: $m = 1, b = 8, k = 0, \sigma = 0.003$.

DPAVIC: $m = 1, b = 5, k = 0, \sigma = 0.01, k_p = 0.2, k_d = 0.05, k_i = 0.001, r = 100, h = 0.01$.

Figure 15 shows the response curves of the end compensation displacement and the contact force. It can be found that when CIC and AVIC are adopted, the overshoot of the

system is large, 10.26% and 7.25%, respectively, and the force control error is 0.336 N and 0.252 N. However, the overshoot and force error of DPAVIC are 1.51%, within ±0.2 N, respectively. Although the system response is slow with the DPAVIC method, the adjustment time is shorter.
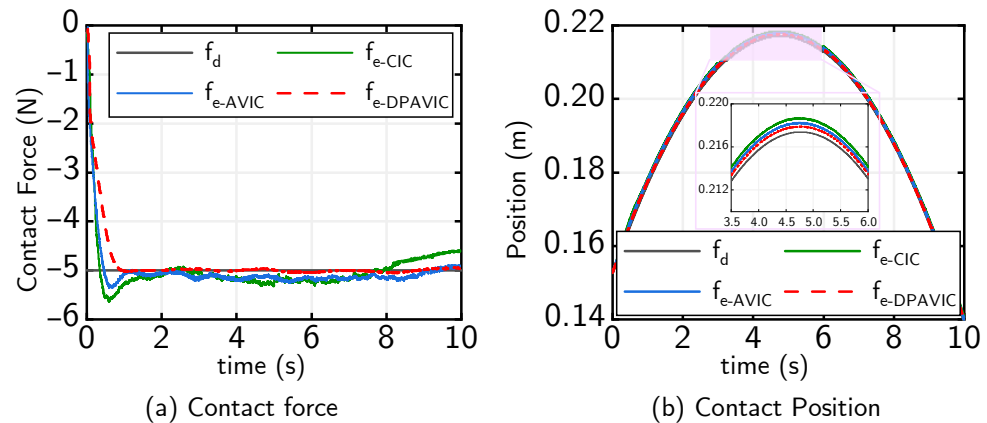

Figure 15. Force control results of large curvature surface.

6.4. Constant Force Grinding Experiment

According to the geometric model of the workpiece surface, the Cartesian space trajectory is planned, the specific grinding pose of the robot end effector is deduced via interpolation with the given feed speed, and the grinding trajectory of the joint space is obtained online with the inverse differential kinematics of the robot. According to the on-site machining requirements, the surface quality of the workpiece should be below Ra 0.3 μm, the reference grinding force is 5 N, and the force fluctuation is ±0.2 N. Table 4 shows the grinding process parameters. The CIC, AVIC, and DPAVIC control parameters are set to the same as the flate force control parameters.

Table 4. Grinding process parameters.

Feed Rate (mm/s)	Grinding Tool Diameter (mm)	Sandpaper (grit)	Grinding Tool Speed (rpm)	(F_d) (N)
15	50	100	3000	−5

As can be seen from Figure 16, the force error in the CIC force tracking control method is far more than ±0.2 N, and the force control result of AVIC is slightly better than that of CIC, while the error of the DPAVIC method stays within ±0.2 N. This proves the ability of the method to improve the precision of force control.
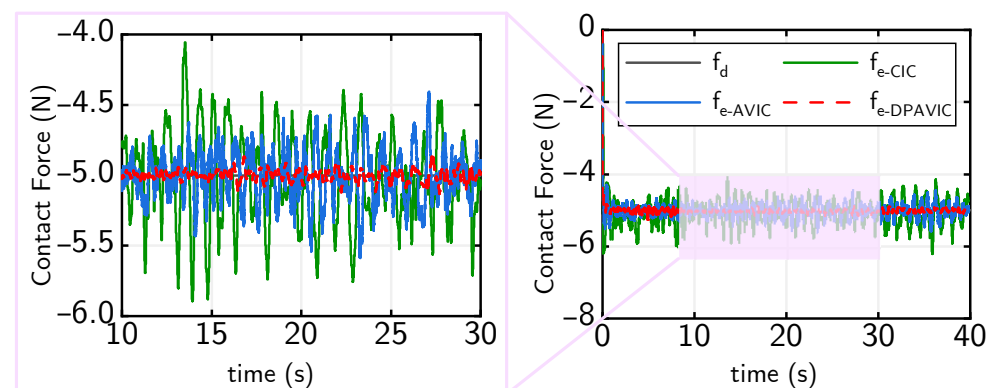

Figure 16. Contact force signal during grinding.

Figure 17 shows the robot grinding process and the surface quality of the workpiece after grinding. To verify the effectiveness of the proposed method for improving machining quality, a JiTai TR200S roughometer was used to measure the surface roughness of the workpiece, a Dino-Lite microscope was used to photograph the grinding surface morphology, and a Mitotoyo Roughness Meter SJ-210 was used to measure surface waviness. As shown in Figure 17b, 10 points on the workpiece surface are selected and the average of three measurements is taken.
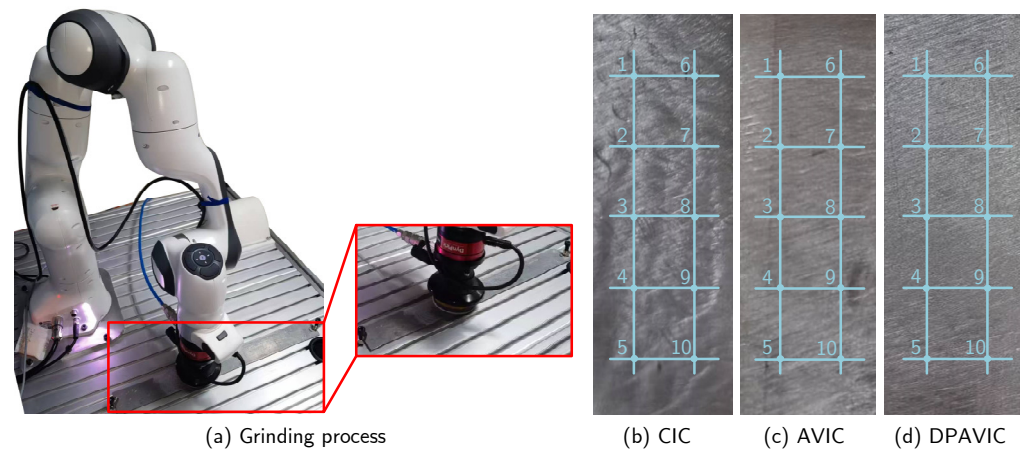

(a) Grinding process　　　　　　　　　(b) CIC　　　(c) AVIC　　　(d) DPAVIC

Figure 17. Workpiece grinding quality.

Figure 18 shows the measured roughness of the workpiece. Compared with the CIC method, the average surface quality of the workpiece is improved from Ra 0.5 μm to Ra 0.218 μm. Figure 19 shows the influence of the three force control methods on the workpiece surface waviness. Figure 19a shows that when using the CIC method, the workpiece surface waviness fluctuates with the grinding force oscillation. Figure 19b shows a slight reduction in waviness with AVIC compared with the CIC method. Figure 19c shows the ability of the DPAVIC method to reduce the workpiece surface waviness, which has the lowest waviness compared with the other two methods. Therefore, the proposed method has the ability to suppress the external disturbance and reduce the force tracking error and fluctuation.
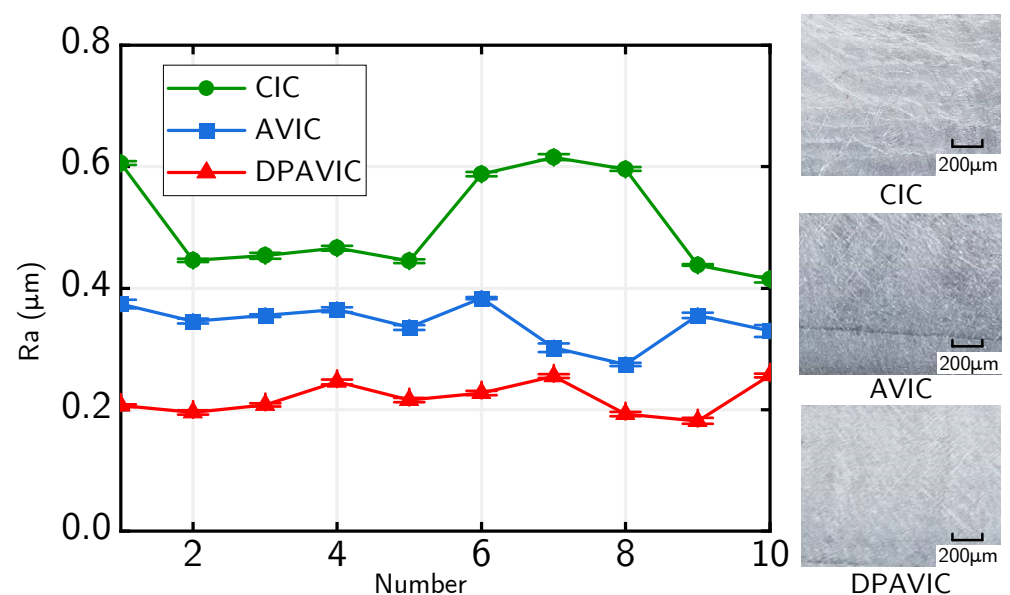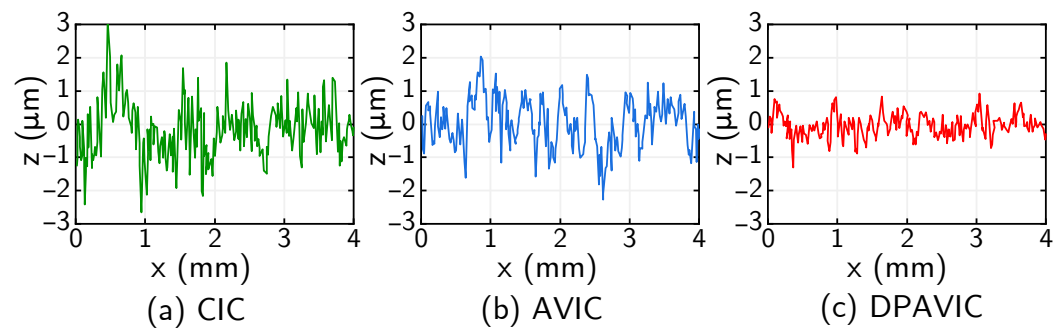

Figure 18. Workpiece surface roughness.

Figure 19. Workpiece surface waviness. (**a**) Effect of CIC on workpiece surface waviness. (**b**) Effect of AVIC on workpiece surface waviness. (**c**) Effect of DPAVIC on workpiece surface waviness.

7. Conclusions

Force control is an important problem in robot contact operation. In order to achieve high efficiency and high-quality robot grinding, a position-based dual PID adaptive variable impedance control method is proposed, PD is used to compensate for the force error, and PID is used to update the impedance parameters to compensate for the environmental disturbance. An overshoot suppression strategy using a nonlinear tracking differentiator is presented to smooth the desired force and reduce the contact force overshoot. The disturbance term of the end force signal is identified using the least square method, and the effect of gravity compensation is verified to reduce the influence of noise on the force control accuracy. The stability, convergence, and effectiveness of the force control algorithm are verified via theoretical analysis, simulations, and experiments. By comparing the results of CIC, AVIC, and DPAVIC with the robot end force control accuracy, the DPAVIC method can be maintained within ± 0.2 N, and it has high anti-interference ability. The surface roughness of the thin-walled workpiece can be improved to Ra 0.218 µm.

In future work, we will consider how to use force sensors to intelligently sense changes in workpiece surface curvature without geometric models and achieve compliant grinding of the workpiece.

Author Contributions: Conceptualization, C.W. and K.G.; data curation, K.G.; formal analysis, C.W. and J.S.; funding acquisition, K.G. and J.S.; investigation, C.W. and K.G.; methodology, C.W.; project administration, J.S.; resources, J.S.; software, C.W. and K.G.; supervision, K.G.; validation, C.W.; visualization, J.S.; writing—original draft, C.W.; writing—review and editing, K.G. and J.S. All authors have read and agreed to the published version of the manuscript.

Institutional Review Board Statement: Not applicable.

Informed Consent Statement: Not applicable.

Data Availability Statement: Not applicable.

Conflicts of Interest: The authors declare no conflict of interest.

Abbreviations

The following abbreviations are used in this manuscript:

ADRC	Active disturbance rejection control
AVIC	Adaptive variable impedance control
CIC	Conventional impedance controller
CNC	Computer numerical control

DPAVIC	Dual PID adaptive variable impedance constant
NTD	Nonlinear tracking differentiator
PID	Proportional-Integral-Derivative controller
PD	Proportional-Derivative controller
6-Dof	Six degrees of freedom

Nomenclature

$\ddot{\hat{e}}$	estimated position disturbance first-order differential
$\ddot{e}$	position perturbation second-order differential
$\ddot{x}_e$	environmental position second-order differential
$\ddot{x}_z$	robot end output acceleration
$\delta \hat{x}_e$	estimated position deviation
Δb	damping compensation
ΔF	force error matrix
Δf	force error in one dimension
Δf_{PD}	force error compensation
Δf_{ss}	force error in one dimension
δ	the parameter update rate
$\dot{\hat{e}}$	estimated position disturbance second-order differential
$\dot{e}$	position perturbation first-order differential
$\dot{x}_e$	environmental position first-order differential
$\dot{x}_z$	robot end output velocity
$\hat{e}$	estimated position disturbance
$\hat{x}_e$	estimated environmental position
λ	the adjustment factor
θ_1, θ_2	the angle around the *x*-axis and *y*-axis of the {D} system
B	the damping matrix of the target impedance
b	the damping of the target impedance
b	the damping parameter of the impedance controller
E	position perturbation matrix
e	position perturbation
F_0	the sensor's zero drift
F_d	desired contact force matrix
f_d	desired contact force
F_e	contact force matrix
F_e	the grinding force
f_e	actual contact force
F_G	the gravity of the grinding tool
F_i	the inertial force
h	the filter factor
K	the stiffness matrix of the target impedance
k	the stiffness of the target impedance
k	the stiffness parameter of the impedance controller
$K(s)$	second-order transfer function
$k(s)$	second-order transfer function
K_e	contact environment stiffness matrix
k_e	contact environment stiffness
M	the mass matrix of the target impedance
m	the mass of the target impedance
m	the mass parameter of the impedance controller
r	the model parameter
t_s	the sampling time
u	nonlinear tracking differentiator
x_1	the target transition signal
x_2	the differential signal of the transition signal
X_c	command trajectory matrix
X_e	environmental position matrix

x_e	environmental position
X_r	reference trajectory matrix
x_r	reference trajectory
X_z	robot end output trajectory matrix
x_z	robot end output trajectory
${}^S F_{mx}, {}^S F_{my}, {}^S F_{mz}$	the force signals of the 6-Dof force sensor
${}^S M_{mx}, {}^S M_{my}, {}^S M_{mz}$	the moment signals of the 6-Dof force sensor

References

1. Zhu, D.; Feng, X.; Xu, X.; Yang, Z.; Li, W.; Yan, S.; Ding, H. Robotic grinding of complex components: A step towards efficient and intelligent machining–challenges, solutions, and applications. *Robot. Comput.-Integr. Manuf.* **2020**, *65*, 101908. [CrossRef]
2. Zhu, W.L.; Beaucamp, A. Compliant grinding and polishing: A review. *Int. J. Mach. Tools Manuf.* **2020**, *158*, 103634. [CrossRef]
3. Ma, K.; Yang, G. Kinematic design of a 3-DOF force-controlled end-effector module. In Proceedings of the 2016 IEEE 11th Conference on Industrial Electronics and Applications (ICIEA), Hefei, China, 5–7 June 2016; pp. 1084–1089.
4. Mu, Y.; Wang, Z.; Zou, L.; Wang, W.; Lv, C.; Wang, A. A novel regional force control strategy based on seven-axis linkage grinding system to improve blade machining accuracy. *J. Manuf. Process.* **2023**, *97*, 235–247. [CrossRef]
5. Solanes, J.E.; Gracia, L.; Muñoz-Benavent, P.; Valls Miro, J.; Perez-Vidal, C.; Tornero, J. Robust hybrid position-force control for robotic surface polishing. *J. Manuf. Sci. Eng.-Trans. ASME* **2019**, *141*, 011013. [CrossRef]
6. Mohammad, A.E.K.; Hong, J.; Wang, D. Design of a force-controlled end-effector with low-inertia effect for robotic polishing using macro-mini robot approach. *Robot. Comput.-Integr. Manuf.* **2018**, *49*, 54–65. [CrossRef]
7. Gracia, L.; Solanes, J.E.; Munoz-Benavent, P.; Miro, J.V.; Perez-Vidal, C.; Tornero, J. Adaptive sliding mode control for robotic surface treatment using force feedback. *Mechatronics* **2018**, *52*, 102–118. [CrossRef]
8. Zhang, H.; Li, L.; Zhao, J.; Zhao, J. The hybrid force/position anti-disturbance control strategy for robot abrasive belt grinding of aviation blade base on fuzzy PID control. *Int. J. Adv. Manuf. Technol.* **2021**, *114*, 3645–3656. [CrossRef]
9. Kakinuma, Y.; Ogawa, S.; Koto, K. Robot polishing control with an active end effector based on macro-micro mechanism and the extended Preston's law. *CIRP Ann.-Manuf. Technol.* **2022**, *71*, 341–344. [CrossRef]
10. Chang, G.; Pan, R.; Xie, Y.; Yang, J.; Yang, Y.; Li, J. Research on constant force polishing method of curved mold based on position adaptive impedance control. *Int. J. Adv. Manuf. Technol.* **2022**, *122*, 697–709. [CrossRef]
11. Rosales, A.; Heikkilä, T. Analysis and Design of Direct Force Control for Robots in Contact with Uneven Surfaces. *Appl. Sci.* **2023**, *13*, 7233. [CrossRef]
12. Zhou, H.; Ma, S.; Wang, G.; Deng, Y.; Liu, Z. A hybrid control strategy for grinding and polishing robot based on adaptive impedance control. *Adv. Mech. Eng.* **2021**, *13*, 16878140211004034. [CrossRef]
13. Xu, X.; Chen, W.; Zhu, D.; Yan, S.; Ding, H. Hybrid active/passive force control strategy for grinding marks suppression and profile accuracy enhancement in robotic belt grinding of turbine blade. *Robot. Comput.-Integr. Manuf.* **2021**, *67*, 102047. [CrossRef]
14. Su, X.; Xie, Y.; Sun, L.; Jiang, B. Constant Force Control of Centrifugal Pump Housing Robot Grinding Based on Pneumatic Servo System. *Appl. Sci.* **2022**, *12*, 9708. [CrossRef]
15. Ke, X.; Yu, Y.; Li, K.; Wang, T.; Zhong, B.; Wang, Z.; Kong, L.; Guo, J.; Huang, L.; Idir, M.; et al. Review on robot-assisted polishing: Status and future trends. *Robot. Comput.-Integr. Manuf.* **2023**, *80*, 102482. [CrossRef]
16. Al-Shuka, H.F.; Leonhardt, S.; Zhu, W.H.; Song, R.; Ding, C.; Li, Y. Active impedance control of bioinspired motion robotic manipulators: An overview. *Appl. Bionics Biomech.* **2018**, *2018*, 8203054. [CrossRef] [PubMed]
17. Fan, C.; Hong, G.S.; Zhao, J.; Zhang, L.; Zhao, J.; Sun, L. The integral sliding mode control of a pneumatic force servo for the polishing process. *Precis. Eng.-J. Int. Soc. Precis. Eng. Nanotechnol.* **2019**, *55*, 154–170. [CrossRef]
18. Ma, Z.; Poo, A.N.; Ang, M.H., Jr.; Hong, G.S.; See, H.H. Design and control of an end-effector for industrial finishing applications. *Robot. Comput.-Integr. Manuf.* **2018**, *53*, 240–253. [CrossRef]
19. Li, J.; Guan, Y.S.; Chen, H.W.; Wang, B.; Zhang, T.; Liu, X.N.; Hong, J.; Wang, D.W.; Zhang, H. A high-bandwidth end-effector with active force control for robotic polishing. *IEEE Access* **2020**, *8*, 169122–169135. [CrossRef]
20. Dai, J.; Chen, C.Y.; Zhu, R.; Yang, G.; Wang, C.; Bai, S. Suppress vibration on robotic polishing with impedance matching. *Actuators* **2021**, *10*, 59. [CrossRef]
21. Nguyen, V.L.; Kuo, C.H.; Lin, P.T. Compliance error compensation of a robot end-effector with joint stiffness uncertainties for milling: An analytical model. *Mech. Mach. Theory* **2022**, *170*, 104717. [CrossRef]
22. Yang, G.; Zhu, R.; Fang, Z.; Chen, C.Y.; Zhang, C. Kinematic design of a 2R1T robotic end-effector with flexure joints. *IEEE Access.* **2020**, *8*, 57204–57213. [CrossRef]
23. Jin, M.; Ji, S.; Pan, Y.; Ao, H.; Han, S. Effect of downward depth and inflation pressure on contact force of gasbag polishing. *Precis. Eng.-J. Int. Soc. Precis. Eng. Nanotechnol.* **2017**, *47*, 81–89. [CrossRef]
24. Chen, Y.; Zhao, J.; Jin, Y. An improved rational Bezier model for pneumatic constant force control device of robotic polishing with hysteretic nonlinearity. *Int. J. Adv. Manuf. Technol.* **2022**, *123*, 665–674. [CrossRef]
25. Pei, G.; Yu, M.; Xu, Y.; Ma, C.; Lai, H.; Chen, F.; Lin, H. An improved PID controller for the compliant constant-force actuator based on BP neural network and smith predictor. *Appl. Sci.* **2021**, *11*, 2685. [CrossRef]

26. Chen, H.; Yang, J.; Ding, H. Robotic compliant grinding of curved parts based on a designed active force-controlled end-effector with optimized series elastic component. *Robot. Comput.-Integr. Manuf.* **2024**, *86*, 102646. [CrossRef]

27. Chen, P.; Zhao, H.; Yan, X.; Ding, H. Force control polishing device based on fuzzy adaptive impedance control. In Proceedings of the Intelligent Robotics and Applications: 12th International Conference, ICIRA 2019, Shenyang, China, 8–11 August 2019; Proceedings, Part IV 12; Springer: Berlin/Heidelberg, Germany, 2019; pp. 181–194.

28. Wei, Y.; Xu, Q. Design of a new passive end-effector based on constant-force mechanism for robotic polishing. *Robot. Comput.-Integr. Manuf.* **2022**, *74*, 102278. [CrossRef]

29. Chen, F.; Zhao, H.; Li, D.; Chen, L.; Tan, C.; Ding, H. Contact force control and vibration suppression in robotic polishing with a smart end effector. *Robot. Comput.-Integr. Manuf.* **2019**, *57*, 391–403. [CrossRef]

30. Wang, Q.; Wang, W.; Ding, X.; Yun, C. A force control joint for robot–environment contact application. *J. Mech. Robot.* **2019**, *11*, 034502. [CrossRef]

31. Chen, C.Y.; Dai, J.; Yang, G.; Wang, C.; Li, Y.; Chen, L. Sensor-based force decouple controller design of macro–mini manipulator. *Robot. Comput.-Integr. Manuf.* **2023**, *79*, 102415. [CrossRef]

32. Xie, F.; Chong, Z.; Liu, X.J.; Zhao, H.; Wang, J. Precise and smooth contact force control for a hybrid mobile robot used in polishing. *Robot. Comput.-Integr. Manuf.* **2023**, *83*, 102573. [CrossRef]

33. Hogan, N. Impedance control: An approach to manipulation. In Proceedings of the 1984 American Control Conference, San Diego, CA, USA, 6–8 June 1984; pp. 304–313.

34. Gu, L.; Huang, Q. Adaptive Impedance Control for Force Tracking in Manipulators Based on Fractional-Order PID. *Appl. Sci.* **2023**, *13*, 10267. [CrossRef]

35. Kawamura, S. Hybrid position/force control of robot manipulators based on learning method. In Proceedings of the 2nd International Conference on Advanced Robotics ICAR 85, Tokyo, Japan, 9–10 September 1985.

36. Gan, Y.; Duan, J.; Chen, M.; Dai, X. Multi-robot trajectory planning and position/force coordination control in complex welding tasks. *Appl. Sci.* **2019**, *9*, 924. [CrossRef]

37. Li, L.; Wang, Z.; Zhu, G.; Zhao, J. Position-based force tracking adaptive impedance control strategy for robot grinding complex surfaces system. *J. Field Robot.* **2023**, *40*, 1097–1114

38. Seraji, H.; Colbaugh, R. Force tracking in impedance control. *Int. J. Robot. Res.* **1997**, *16*, 97–117. [CrossRef]

39. Bilal, M.; Akram, M.N.; Rizwan, M. Adaptive Variable Impedance Control for Multi-axis Force Tracking in Uncertain Environment Stiffness with Redundancy Exploitation. *Control Eng. Appl. Inform.* **2022**, *24*, 35–45.

40. Jia, H.; Lu, X.; Cai, D.; Xiang, Y.; Chen, J.; Bao, C. Predictive Modeling and Analysis of Material Removal Characteristics for Robotic Belt Grinding of Complex Blade. *Appl. Sci.* **2023**, *13*, 4248. [CrossRef]

41. Kronander, K.; Billard, A. Stability considerations for variable impedance control. *IEEE Trans. Robot.* **2016**, *32*, 1298–1305. [CrossRef]

42. Cao, H.; Chen, X.; He, Y.; Zhao, X. Dynamic adaptive hybrid impedance control for dynamic contact force tracking in uncertain environments. *IEEE Access.* **2019**, *7*, 83162–83174. [CrossRef]

43. Wang, G.; Deng, Y.; Zhou, H.; Yue, X. PD-adaptive variable impedance constant force control of macro-mini robot for compliant grinding and polishing. *Int. J. Adv. Manuf. Technol.* **2023**, *124*, 2149–2170. [CrossRef]

44. Wahballa, H.; Duan, J.; Dai, Z. Constant force tracking using online stiffness and reverse damping force of variable impedance controller for robotic polishing. *Int. J. Adv. Manuf. Technol.* **2022**, *121*, 5855–5872. [CrossRef]

45. Wang, Q.; Wang, W.; Zheng, L.; Yun, C. Force control-based vibration suppression in robotic grinding of large thin-wall shells. *Robot. Comput.-Integr. Manuf.* **2021**, *67*, 102031. [CrossRef]

46. Lee, C.H.; Wang, W.C. Robust adaptive position and force controller design of robot manipulator using fuzzy neural networks. *Nonlinear Dyn.* **2016**, *85*, 343–354. [CrossRef]

47. Irawan, A.; Nonami, K. Optimal impedance control based on body inertia for a hydraulically driven hexapod robot walking on uneven and extremely soft terrain. *J. Field Robot.* **2011**, *28*, 690–713. [CrossRef]

48. Ranko, Z.; Angel, V.F.; Pedro, G.G.; Angel, L.G. An architecture for robot force and impact control. In Proceedings of the 2006 IEEE Conference on Robotics, Automation and Mechatronics, Bangkok, Thailand, 7–9 June 2006; pp. 1–6.

49. Roveda, L.; Pedrocchi, N.; Vicentini, F.; Tosatti, L.M. An interaction controller formulation to systematically avoid force overshoots through impedance shaping method with compliant robot base. *Mechatronics* **2016**, *39*, 42–53. [CrossRef]

50. Duan, J.; Gan, Y.; Chen, M.; Dai, X. Adaptive variable impedance control for dynamic contact force tracking in uncertain environment. *Robot. Auton. Syst.* **2018**, *102*, 54–65. [CrossRef]